

Newly Synthesized Elements and Pristine Dust in the Cassiopeia A Supernova Remnant¹

R. G. Arendt², E. Dwek, and S. H. Moseley
Laboratory for Astronomy and Solar Physics,
Code 685, NASA GSFC, Greenbelt, MD 20771;

arendt@stars.gsfc.nasa.gov, edwek@stars.gsfc.nasa.gov, moseley@stars.gsfc.nasa.gov

ABSTRACT

Spectroscopic observations at 2.4 – 45 μm of the young supernova remnant Cas A with the *Infrared Space Observatory (ISO)* Short Wavelength Spectrometer (SWS) reveal strong emission lines of O, Ne, Si, S, and Ar. These lines are observed at high velocities (several 10^3 km s^{-1}), and are therefore associated with the supernova ejecta known as the fast-moving knots (FMKs). Continuum emission from dust is also seen in the Cas A spectrum. The continuum strength is spatially well correlated with the O and Ar line strengths, indicating that the dust emission also arises from the FMKs. The dust continuum has an emission feature at $\sim 22 \mu\text{m}$ which cannot be fit by typical astronomical silicates, but can be fit with a particular class of silicate minerals. This suggests that the dust in Cas A is silicate material that has freshly condensed from the Cas A ejecta into a mineral form that is uncharacteristic of typical ISM dust grains.

Subject headings: infrared: ISM: continuum — infrared: ISM: lines and bands — dust, extinction — ISM: individual (Cassiopeia A) — supernova remnants

1. INTRODUCTION

Infrared (IR) observations of supernova remnants (SNRs) primarily reveal the thermal continuum emission of shock-heated dust (Dwek & Arendt 1992; and references therein). For most remnants, this dust is typical interstellar dust that has been swept up in the expanding supernova blast wave. Only the very youngest SNRs offer the possibility of observing dust that has formed from the metal-enriched ejecta of the supernova itself, before it is dispersed and mixed into the general ISM. The dust content of SNRs is not directly observable in any other wavelength regime. The IR portion of the spectrum also contains ground-state fine-structure lines from neutral to moderately ionized species of atoms from carbon to nickel. Observations of these fine structure lines offer the capability of probing density and temperature regimes not represented by the commonly observed optical transitions. Another distinct advantage of IR observations is that extinction is much lower at IR than optical or UV wavelengths.

The earliest airborne and ground based searches for IR emission from the Cas A supernova remnant (SNR) only managed to set upper limits on the intensity of the IR emission (Wright et al. 1980, Dinerstein et al. 1982). Observations with the *IRAS* satellite, launched in 1983, provided the first clear detection of

¹Based on observations with *ISO*, an ESA project with instruments funded by ESA Member States (especially the PI countries: France, Germany, the Netherlands and the United Kingdom) and with the participation of ISAS and NASA

²Raytheon STX

Cas A at IR wavelengths. These measurements of the mid-IR emission in broad bands at 12, 25, 60 and 100 μm enabled several detailed investigations into the nature of the heating mechanism of the dust within the remnant (Dwek et al. 1987a, Braun 1987). However the *IRAS* data lacked the spatial resolution to reveal more than the gross distribution of dust within the SNR. The *IRAS* data also lacked the spectral resolution needed to determine the amount of line emission that might be contributing in the mid-IR. Subsequent observations by (Dinerstein et al. 1987) detected weak line emission of [S IV] at 10.4 μm . Greidanus & Strom (1991) made a higher resolution ground-based map of the northern part of the remnant at 20 μm . This map reveals clumpy IR emission that does not appear to be strongly correlated with either the optical or X-ray emission. With the advent of the *ISO*, IR observations with high spatial and spectral resolution are available. An ISOCAM map of Cas A at 10.7 – 12 μm (Lagage et al. 1996) shows emission that is distributed in a manner similar to the de-extincted X-ray emission, or the radio emission. Much of the brightest emission correlates with line emission from high velocity ejecta within the SNR, leading Lagage et al. (1996) to propose that the observed emission arises from dust that has formed in the knots of supernova ejecta, and is now being heated as the knots are evaporating into the hot gas of the supernova blast wave (Dwek & Werner 1981).

In this paper we present analysis of IR observations of the young Cas A SNR. The 2.4 – 45 μm data acquired with the *ISO* Short Wavelength Spectrometer are described in §2. Section 3 is devoted to analysis of the observed line and continuum emission. Section 4 discusses the implications for mixing of the supernova ejecta, and the formation of dust within the ejecta.

2. DATA AND REDUCTION

The *ISO* data used in this study were obtained using the Short Wavelength Spectrometer (SWS) (de Graauw et al. 1996). All observations were collected in the AOT 1 observing mode which provided moderate resolution ($\lambda/\Delta\lambda \sim 500$) spectra over the entire 2.38 – 45.2 μm wavelength range of the instrument. Ten locations in the SNR were targeted as listed in Table 1. The “North” fields (N1 – N6) are located in the northern rim of the remnant where many optical knots are seen, the X-ray and radio emission are bright, and IR emission is strong. Regions N1 – N4 step across the area of the brightest optical knots. Region N5 was intended to sample emission from ejecta at larger radii from the expansion center, but was observed for a shorter interval than the other regions due to time constraints. Region N6 was aimed at a knot identified by Fesen (1990; knot “D”) as a potential source of [Ne III] emission. The “South” fields (S1 - S5) are in the southeastern portion of the remnant at a location where the 25 μm emission observed with *IRAS* and the X-ray emission are fairly strong (Dwek et al. 1987a), but the optical and radio emission are relatively weak. (Region S3 was not observed due to time constraints.) The data have been processed through Off-Line Processing (OLP) 6.11 and 6.31, with further identification and exclusion of bad data and averaging using ISAP³ and our own similarly functional software.

Background emission in the spectra is apparently very weak and thus has not been subtracted for any of the spectra shown here. Some of the South regions show little or no line or continuum emission from either the SNR or the background. Modeling of the zodiacal light (Kelsall et al. 1998), the strongest background component at mid-IR wavelengths, indicates that this emission from local interplanetary dust should contribute less than 0.25 Jy at 25 μm in the SWS aperture. Similarly, the data have not been

³The ISO Spectral Analysis Package (ISAP) is a joint development by the LWS and SWS Instrument Teams and Data Centers. Contributing institutes are CESR, IAS, IPAC, MPE, RAL and SRON.

corrected for extinction. Using either the Mathis (1990) extinction law or that calculated by Drain & Lee (1984), and the visual extinction estimate of $A_V = 4.3$ mag (Searle 1971), the largest extinction in the mid-IR should be $\tau \approx 0.28$, found at the wavelength of the $10 \mu\text{m}$ silicate feature. This amount of extinction would reduce the observed intensities by $\sim 24\%$ at $\sim 10 \mu\text{m}$. At other wavelengths the extinction generally reduces the observed intensities by less than 10 %. Correction for this would have little effect on the results presented here, and would introduce additional sources of error related to the accuracy of the V -band extinction and its extrapolation to IR wavelengths, and the uniformity of extinction across the remnant.

We had previously obtained spectra of Cas A at three locations using the KAO (Moseley et al. 1993). These data cover a smaller wavelength range at lower resolution than the SWS data. Therefore, their main utility is to provide confirmation of the spectral features and relative calibration of the SWS data. The highest quality KAO data were obtained at a location roughly matching that of Region N1. The other observed locations, at regions S1 and at the optically bright Filament 1 of Baade & Minkowski (1954), showed no detectable emission.

3. ANALYSIS

3.1. Line Emission

Selected portions of the SWS spectra of the ten observed fields are illustrated in Figure 1. The panels in each row of Figure 1, cover a wavelength range of exactly $\pm 4\%$ centered on the rest wavelength of a particular fine structure transition. Each row is selected to cover the region of a different transition. In this depiction, different transitions observed at the same radial velocity in a given field should be aligned in each column.

The most prominent line in the spectra is the [O IV] $25.89 \mu\text{m}$ line (seventh row of Fig. 1) which is seen in all but the S4 spectrum. As well as being intrinsically strong, this line falls in a region where the SWS sensitivity is good. The dashed lines running vertically in each column of Figure 1 are drawn at the location each transition should appear if it occurs at the same radial velocity as the [O IV] emission in the field. In Region N1 there are distinct red- and blueshifted components. The [Ar II] $6.98 \mu\text{m}$ line (first row of Fig. 1) is the second most prevalent line observed. Like the [O IV] line it benefits from being intrinsically strong and in a spectral region where the SWS sensitivity is good. The radial velocities of the [Ar II] and the [O IV] lines are fairly close. This agreement allows us to discriminate between the $25.89 \mu\text{m}$ [O IV] line and the $25.99 \mu\text{m}$ [Fe II] line. If the $26 \mu\text{m}$ line were emitted by Fe II, then in Region N1 we would have the unlikely situation where the iron ejecta would be moving $\sim 10^3 \text{ km s}^{-1}$ faster than the argon ejecta on the front side of the SNR, but $\sim 10^3 \text{ km s}^{-1}$ slower than the argon on the back side of the remnant. Almost all other lines that are observed match the [O IV] and [Ar II] velocities. The exception is the apparent [Si II] line in the N1 region. All of the detected lines correspond to ionized species that are created by overcoming n -th ionization potentials in the range of 8 - 55 eV, and that have cosmic elemental abundances at least as great as argon. The only species with similar abundances and ionizations with lines in the SWS range that that are not observed are H I and Fe II, Fe III, and Fe V.

All lines were fit for a baseline and a Gaussian line profile, to determine radial velocities, line widths, and fluxes. These results are presented in Table 2. In most regions the radial velocities are in excess of 1000 km s^{-1} . The velocity uncertainties quoted in Table 2 are the formal uncertainties of the fits, and do not account for systematic errors that may influence the apparent line positions and widths. This indicates that the line emission is arising from fast moving ejecta (e.g. the FMKs) and not relatively

Table 1. Observed Locations

Field	α (J2000)	δ (J2000)	Roll Angle (deg)	SWS Speed
N1	23 23 29.9	+58 50 22.8	67.26	2
N2	23 23 26.9	+58 50 22.7	234.89	2
N3	23 23 23.9	+58 50 22.7	234.90	2
N4	23 23 20.9	+58 50 22.7	234.91	2
N5	23 23 29.9	+58 50 52.8	67.24	1
N6	23 23 25.7	+58 50 03.7	67.52	2
S1	23 23 38.1	+58 48 30.9	234.87	2
S2	23 23 38.1	+58 49 00.9	234.89	2
S4	23 23 38.1	+58 48 00.9	231.09	2
S5	23 23 35.0	+58 48 30.8	234.90	2

Table 2. Cas A Line Fluxes

Region	Line	Rest Wavelength, λ_0 (μm)	Wavelength, λ (μm)	Velocity, v (km s^{-1})	Peak Flux Density, S_ν (Jy)	Width, σ (μm)	Flux, F ($10^{-12} \text{ erg s}^{-1} \text{ cm}^{-2}$)
N1	[Ar II]	6.985274	6.944 \pm 0.001	-1753 \pm 32	11.17 \pm 0.73	0.0107 \pm 0.0007	18.7 \pm 1.7
N1	[Ar II]	6.985274	7.052 \pm 0.002	+2874 \pm 102	2.430 \pm 0.28	0.0172 \pm 0.0024	6.3 \pm 1.1
N1	[Ar III]	8.99138	8.932 \pm 0.002	-1988 \pm 72	1.999 \pm 0.90	0.0090 \pm 0.0032	1.7 \pm 1.0
N1	[S IV]	10.5105	10.45 \pm 0.005	-1842 \pm 129	2.904 \pm 0.64	0.0212 \pm 0.0051	4.2 \pm 1.4
N1	[Ne II]	12.81355	12.73 \pm 0.001	-1944 \pm 28	7.613 \pm 0.45	0.0212 \pm 0.0013	7.5 \pm 0.6
N1	[Ne III]	15.5551	15.45 \pm 0.003	-2022 \pm 58	3.813 \pm 0.73	0.0116 \pm 0.0034	1.4 \pm 0.5
N1	[O IV]	25.8903	25.75 \pm 0.003	-1620 \pm 37	18.10 \pm 1.14	0.0449 \pm 0.0030	9.2 \pm 0.8
N1	[O IV]	25.8903	26.12 \pm 0.005	+2625 \pm 61	8.649 \pm 0.67	0.0591 \pm 0.0058	5.6 \pm 0.7
N1	[Si II]	34.8152	34.99 \pm 0.009	+1508 \pm 79	17.24 \pm 1.54	0.1156 \pm 0.0092	12.2 \pm 1.5
N2	[Ar II]	6.985274	6.956 \pm 0.001	-1239 \pm 58	3.952 \pm 0.48	0.0112 \pm 0.0016	6.9 \pm 1.3
N2	[O IV]	25.8903	25.77 \pm 0.008	-1436 \pm 94	4.917 \pm 0.35	0.1109 \pm 0.0086	6.2 \pm 0.6
N3	[Ar II]	6.985274	6.941 \pm 0.001	-1883 \pm 32	11.46 \pm 0.64	0.0133 \pm 0.0006	23.8 \pm 1.8
N3	[Ar III]	8.99138	8.938 \pm 0.002	-1763 \pm 71	2.949 \pm 0.39	0.0137 \pm 0.0021	3.8 \pm 0.8
N3	[S IV]	10.5105	10.44 \pm 0.002	-2021 \pm 62	3.869 \pm 0.52	0.0145 \pm 0.0021	3.9 \pm 0.8
N3	[Ne II]	12.81355	12.72 \pm 0.005	-2230 \pm 126	3.041 \pm 0.45	0.0208 \pm 0.0054	2.9 \pm 0.9
N3	[S III]	18.7130	18.59 \pm 0.002	-1998 \pm 34	9.499 \pm 0.76	0.0200 \pm 0.0021	4.1 \pm 0.5
N3	[O IV]	25.8903	25.71 \pm 0.002	-2100 \pm 25	22.05 \pm 0.99	0.0549 \pm 0.0019	13.8 \pm 0.8
N3	[S III]	33.4810	33.28 \pm 0.024	-1805 \pm 217	6.122 \pm 1.40	0.1072 \pm 0.0243	4.5 \pm 1.4
N4	[Ar II]	6.985274	6.985 \pm 0.002	-22 \pm 67	3.643 \pm 0.29	0.0196 \pm 0.0015	11.0 \pm 1.2
N4	[O IV]	25.8903	25.89 \pm 0.007	-58 \pm 77	6.525 \pm 0.34	0.1244 \pm 0.0065	9.1 \pm 0.7
N4	[Si II]	34.8152	34.87 \pm 0.014	+454 \pm 117	14.64 \pm 3.09	0.0648 \pm 0.0136	5.9 \pm 1.7
N5	[O IV]	25.8903	26.08 \pm 0.011	+2230 \pm 130	3.555 \pm 0.57	0.0548 \pm 0.0117	2.2 \pm 0.6
N6	[Ar II]	6.985274	6.922 \pm 0.002	-2722 \pm 68	3.956 \pm 0.77	0.0090 \pm 0.0016	5.6 \pm 1.5
N6	[Ar III]	8.99138	8.908 \pm 0.007	-2780 \pm 223	1.224 \pm 0.28	0.0248 \pm 0.0078	2.9 \pm 1.1
N6	[Ne II]	12.81355	12.68 \pm 0.003	-3150 \pm 60	4.738 \pm 0.46	0.0212 \pm 0.0023	4.7 \pm 0.7
N6	[O IV]	25.8903	25.64 \pm 0.002	-2949 \pm 25	11.11 \pm 0.85	0.0380 \pm 0.0021	4.8 \pm 0.5
S1	[O IV]	25.8903	25.88 \pm 0.005	-88 \pm 59	6.079 \pm 0.77	0.0434 \pm 0.0056	3.0 \pm 0.5
S2	[O IV]	25.8903	26.01 \pm 0.007	+1385 \pm 77	3.298 \pm 0.37	0.0614 \pm 0.0073	2.2 \pm 0.4
S5	[O IV]	25.8903	25.91 \pm 0.008	+283 \pm 88	3.528 \pm 0.48	0.0578 \pm 0.0091	2.3 \pm 0.5

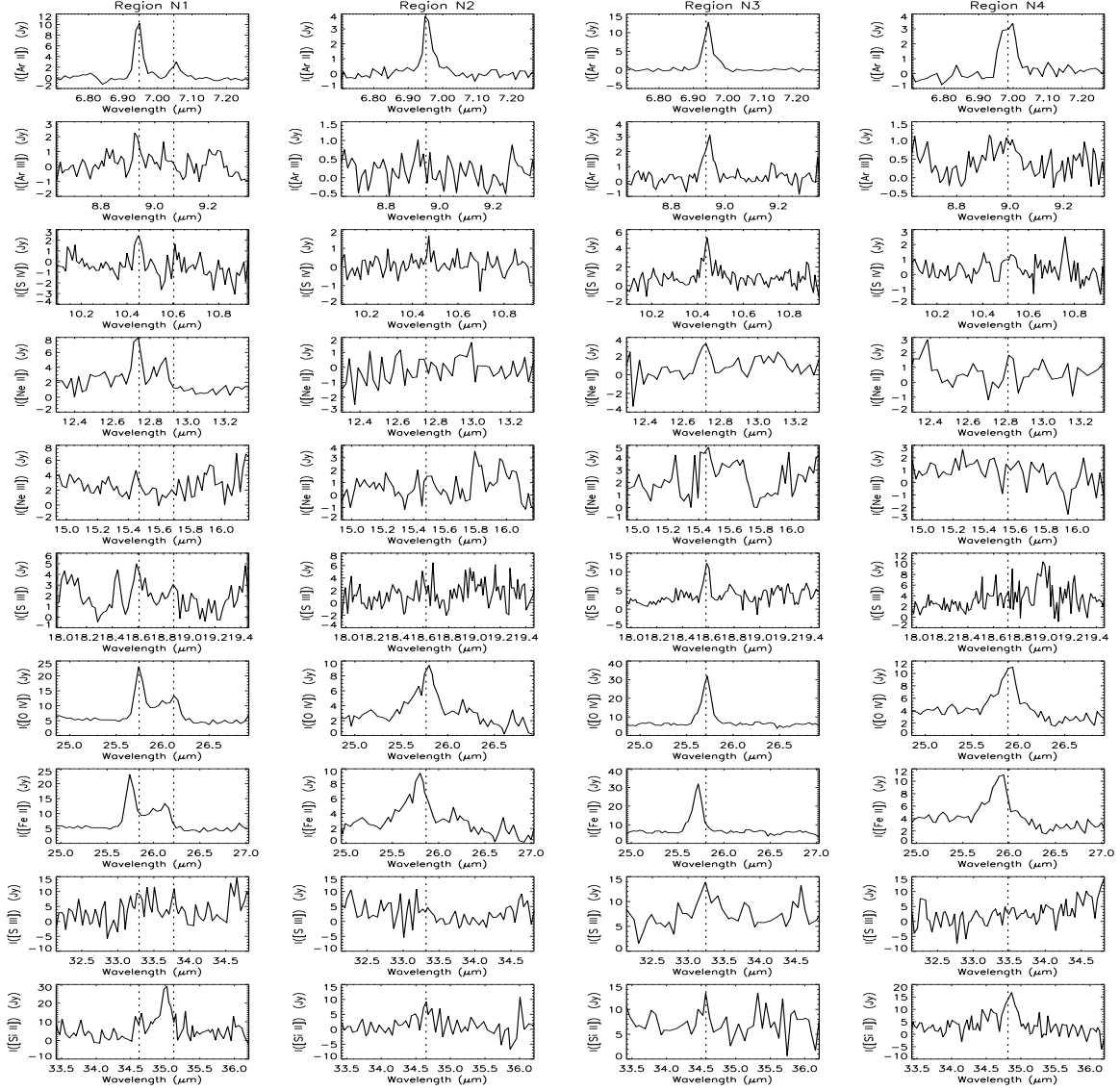


Fig. 1.— The spectra of Cas A at the observed locations are shown in the regions of selected fine-structure emission lines. Each column corresponds to a single location in the Cas A remnant. Each row highlights a particular line. The vertical dashed lines indicated the expected location of fine structure lines if they are found at the same radial velocity as the 26 μm [O IV] line(s) in each observed region.

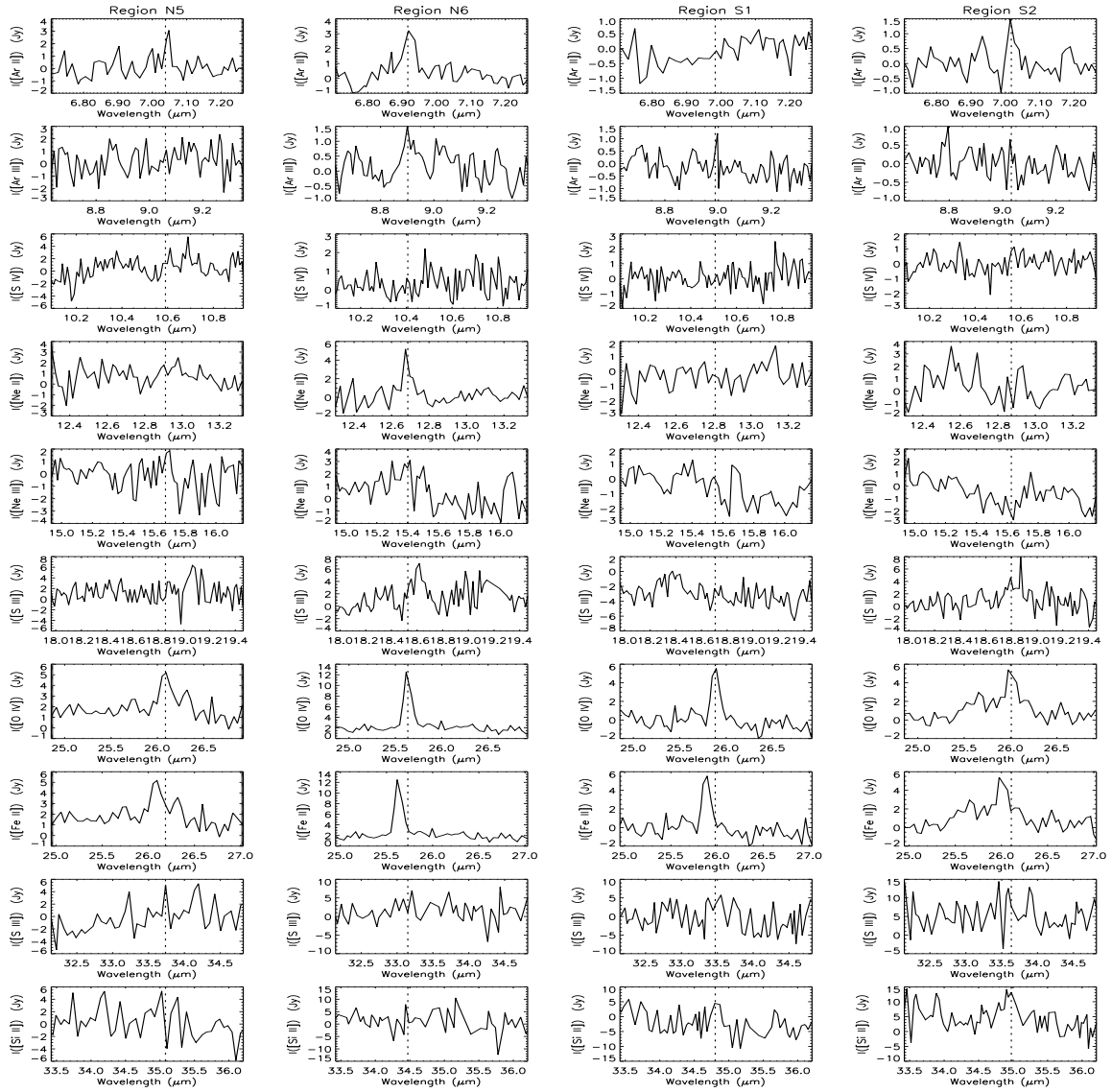


Fig. 1.— CONTINUED

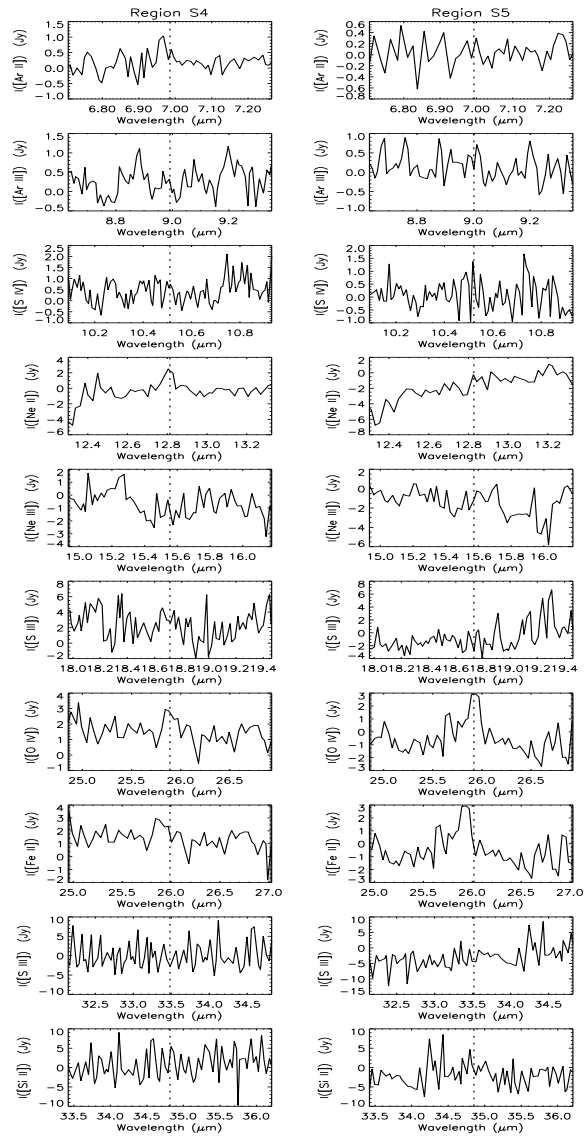


Fig. 1.— CONTINUED

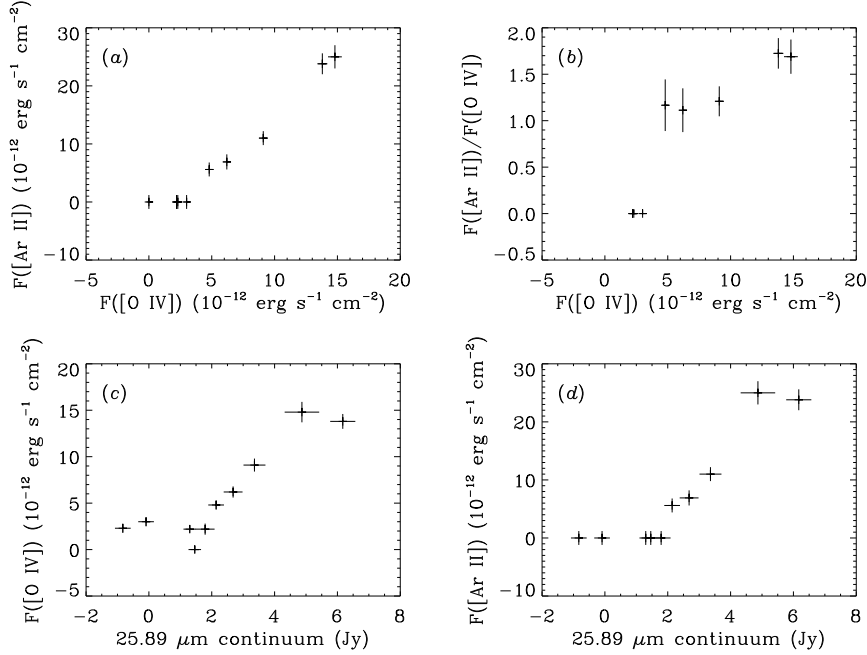


Fig. 2.— Correlations of (a) [Ar II] line flux vs. [O IV] line flux, (b) [Ar II]/[O IV] flux ratio vs. [O IV] line flux, (c) [O IV] line flux vs. continuum flux density, and (d) [Ar II] line flux vs. continuum flux density,

slow swept up material such as the quasistationary flocculi (QSFs) with typical velocities of several 10^2 km s^{-1} . The velocities of the emission can be used to identify corresponding knots which have been studied at optical wavelengths. Comparison to the observations of Hurford & Fesen (1996) suggests the following correspondence between emission in our observed regions and their fast moving knots: Region N1 ($v = -1700 \text{ km}^{-1}$) \approx FMK 2, Region N3 \approx FMK 5, and Region N6 \approx FMK 4. The line ratios observed in the N regions are similar to those observed with other instruments aboard *ISO* (Lagage et al. 1996; Tuffs et al. 1998).

The [Ar II] emission is strongly correlated with the [O IV] emission in intensity as well as velocity as shown in Figure 2a. Figure 2b shows that the ratio of $F([\text{Ar II}]) / F([\text{O IV}])$ may increase as a function of intensity. However, regions in the southeast portion of the remnant seem to exhibit the [O IV] emission without corresponding [Ar II] emission.

The ratio of 18.71 μm and 33.48 μm [S III] lines seen in Region N3 can be used as a density diagnostic (e.g. Houck et al. 1984). The identification and the intensity of the 33.48 μm line is uncertain, but if reliable, the indicated electron density of the emitting region is $n_e = 600_{-400}^{+700} \text{ cm}^{-3}$. Ratios of [Ne III] (15.56 and 36.01 μm) and [Ar III] (8.99 and 21.83 μm) lines are also density sensitive (Butler & Mendoza 1984; Keenan & Conlon 1993), but for these ionic species one line of each pair is too weak to be observed in the SWS data.

Ratios of the [Ar III] 7135Å and 8.99 μm lines can be used as a temperature indicator (Keenan & Conlon 1993). Using the Hurford & Fesen (1996) intensities for the 7135Å [Ar III] lines, we find electron temperatures of $T_e \approx 11,000, 4800, \text{ and } 5500 \text{ K}$ for Regions N1, N3, and N6 respectively. The temperatures are highly uncertain, and are consistently lower than the $T_e \simeq 20,000 - 25,000 \text{ K}$ that Hurford & Fesen (1996) derive from the ratios of the optical [O III] lines. This difference may be explained if some of the optical emission is missing because the knots are wider than the 2"5 slit used for the optical spectroscopy, or if the IR emission arises from a blend of several knots. Alternatively, it may be that the [Ar III] and [O III] are tracing different regions of the shocked FMK.

Estimates of the mass in each of the ionic species observed have been made assuming that the electron temperature is $T_e = 10^4 \text{ K}$ and the electron density is $n_e = 1000 \text{ cm}^{-3}$, which is at least an order of magnitude below the critical densities at which the observed IR transitions would be collisionally deexcited (Table 3). At densities below the critical densities, the derived masses are proportional to $T_e^{0.5} e^{hc/\lambda k T_e} n_e^{-1}$.

3.2. Continuum Emission

3.2.1. Dust Composition and Mass

The IR spectra from the various regions also exhibit continuum emission with an intensity that varies as widely as the line intensities. While some fraction of the continuum emission of the SNR should be synchrotron radiation, the bright continuum emission that is detected in the SWS data is far too strong to be an extension of the radio power-law spectrum through the IR wavelengths (e.g. Mezger et al. 1986; Dwek et al. 1987a). The continuum emission also exhibits a shape that strongly indicates that it is thermal emission from dust grains within the SNR.

We find that the continuum flux density at 26 μm (the baseline flux density underlying the fit to the [O IV] lines) is well correlated with the line intensities of both [O IV] and [Ar II] (Figures 2c and 2d). This suggests that the dust that produces the observed continuum emission is associated with the same fast moving ejecta which produces the line emission. A similar correlation between the [S IV] 10.5 μm emission and the 11.3 μm continuum has led Lagage et al. (1996) to the same conclusion.

Table 3. Derived Masses in Bright Regions

Ionic Species	Mass ^a ($10^{-5} M_{\odot}$)		
	N1 ($v < 0$)	N1 ($v > 0$)	N3
O IV	2.3	1.4	3.4
Ne II	19	...	7.5
Ne III	2.7
Si II	...	2.9 ^b	...
S III	1.1
S IV	0.34	...	0.32
Ar II	27	9.2	35
Ar III	1.3	...	2.8
Dust	0.28

^aIonic masses assume $n_e = 1000 \text{ cm}^{-3}$, $T_e = 10^4 \text{ K}$, and that collisional deexcitation is unimportant.

^bVelocity differs from [O IV] and [Ar II] emission

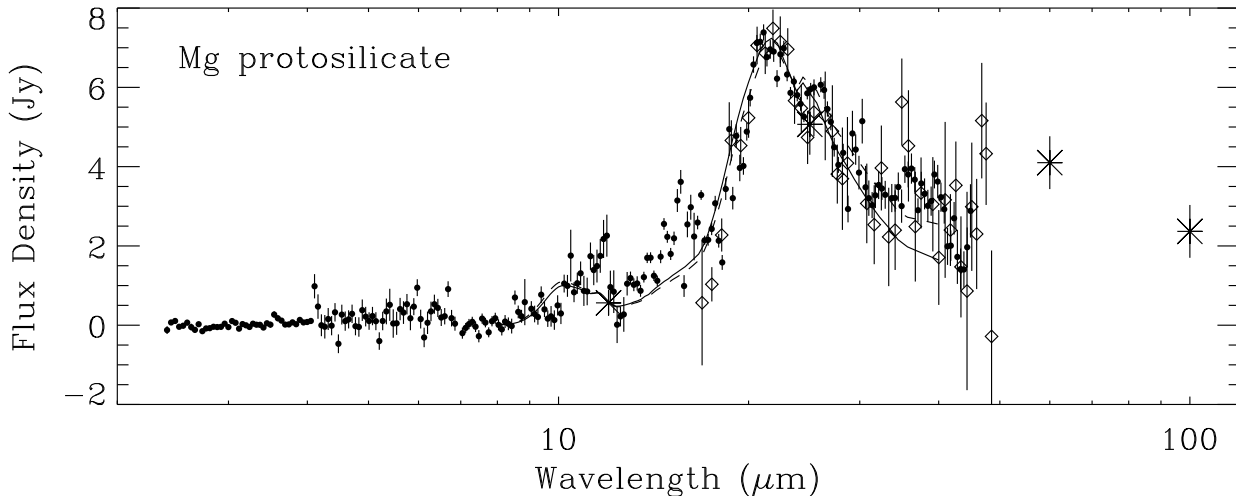


Fig. 3.— The *ISO* SWS spectrum for the N3 region (dots with 1σ error bars) smoothed to a resolution of $\lambda/\Delta\lambda = 200$. The KAO data (normalized to the SWS data) are indicated by diamonds. The solid line is the best fit spectrum for dust with a Mg protosilicate emissivity (Dorschner et al. 1980; sample F), for which $T_d = 169$ K. The dashed line is the model spectrum if the dust is stochastically heated (§3.2.3). The broadband *IRAS* data at 12, 25, 60 and 100 μm integrated over the entire SNR are scaled by a factor of 40 and plotted as stars.

In the following, we will concentrate on the analysis of the region N3, which was the brightest of the regions and has the cleanest spectrum. Other than the changes in intensity, it is not clear that any of the other continuum spectra are different from that of region N3. The continuum spectrum after clipping the observed spectral lines and averaging to a resolution of $R = \lambda/\Delta\lambda = 200$ is shown in Figure 3. Also shown is the KAO spectrum, arbitrarily scaled to match. The KAO and *ISO* results appear to be in very good agreement. Both data sets clearly indicate a spectrum that rises quickly, peaks at 21 – 22 μm and then fades more slowly at longer wavelengths. The *IRAS* flux densities at 12, 25, 60, and 100 μm normalized to roughly match the 25 μm flux density of Region N3 are shown in Fig. 3.

The peak in this spectrum cannot be fit with single temperature blackbody emission from dust with a λ^{-2} emissivity. The line drawn through Figure 3 indicates a single dust temperature fit to the SWS spectrum for dust grains with an emissivity taken to be that of Mg protosilicate (Dorschner et al. 1980). The derived dust temperature for this fit is 169 K, and can vary by ~ 40 K without producing a distinctly poor fit to the data. The best fitting spectra for other potential grain compositions are illustrated in Figure 4. Blackbody emission, graphite, and silicate grains with Draine & Lee (1984) optical constants provide relatively poor fits. The 22 μm peak in the Cas A spectrum is at a wavelength too long for the typical astronomical silicate, which is usually stated to have an emission feature at ~ 18 μm . Of the various silicate optical properties which have been measured and published, the only ones which produced good fits to the Cas A spectrum were the protosilicates measured by Dorschner et al. (1980). For the SWS data at region N3, the Fe protosilicate emissivity provides a slightly better fit than the Mg protosilicate. Considering only the KAO data, the Mg protosilicate provides the better fit. Ca protosilicate has a emission feature at 22 μm , but it is narrower than that of the other protosilicates and the data. Iron oxide (FeO) has also has a sharp emission feature near 22 μm (Henning et al. 1995). The feature can be broadened to produce a fair

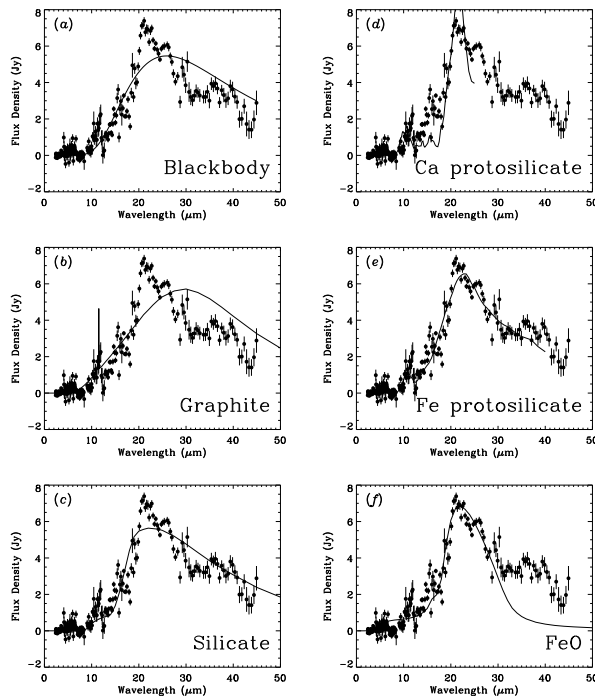


Fig. 4.— The same SWS data for Region N3 as in Figure 3, this time fitted by (a) a 112 K blackbody spectrum modified by a λ^{-2} emissivity, (b) a 188 K graphite spectrum (Draine & Lee 1984), (c) a 124 K astronomical silicate spectrum (Draine & Lee 1984), (d) a 184 K Ca protosilicate spectrum (Dorschner et al. 1980; sample A), (e) a 165 K Fe protosilicate spectrum (Dorschner et al. 1980; sample E), and (f) a 396 K FeO spectrum calculated for a continuous distribution of ellipsoidal grains (Henning et al. 1995).

fit to the data if it is assumed that, rather than spherical grains, a continuous distribution of ellipsoidal grains (CDE approximation; Bohren & Huffman, 1983) is present. However, FeO grains cannot account for both the 22 μ m feature and the continuum emission at $> 30 \mu$ m.

The *IRAS* measurements shown in Figure 3, show an excess at 60 and 100 μ m over the extrapolated spectra that fit the 22 μ m emission peak (Figs. 3 or 4e,f). This indicates the presence of cooler dust within the SNR. However, since the *IRAS* flux densities are for the integrated emission of the SNR, it is not clear whether the cooler dust resides in the FMKs or elsewhere in the SNR.

The mass of hot (~ 170 K) dust observed in Cas A is given by

$$M_{dust} = \frac{S_\nu d^2}{B_\nu(T_d) \kappa_\nu} \quad (1)$$

where S_ν is the observed flux density, d is the distance to Cas A, $B_\nu(T_d)$ is the Planck blackbody function evaluated at the dust temperature T_d , and $\kappa_\nu = 3Q/4a\rho$ is the mass absorption coefficient for the dust. For region N3, $S_\nu(26 \mu\text{m}) = 6.2$ Jy, $d = 3.4$ kpc (Reed et al. 1995), $T_d = 169$ K, and $\kappa_\nu(26 \mu\text{m}) = 1332 \text{ cm}^2 \text{ g}^{-1}$ for Mg protosilicate (Dorschner et al. 1980), yielding $2.8 \times 10^{-6} M_\odot$ of dust in the region. Comparison to the mass of the gas in Region N3 (Table 3) suggests that as much as 2% of the Si ejecta in the FMKs has been condensed into dust assuming that Mg protosilicate is $\sim 25\%$ Si by mass, and all the Si is traced by the observed dust and [Si II] emission.

The total mass of hot dust in the SNR can be roughly estimated by scaling this dust mass by the ratio of the total flux density of Cas A to the flux density of this region. With a total flux density from *IRAS* observations of ~ 164 Jy (Arendt 1989) at $25 \mu\text{m}$, we estimate that Cas A contains $\sim 7.7 \times 10^{-5} M_{\odot}$ of hot dust. The mass derived here is a factor of 10 – 100 lower than previous estimates of $0.5 - 7 \times 10^{-3} M_{\odot}$ based on *IRAS* observations (Mezger et al. 1986; Braun 1987; Dwek et al. 1987a; Greidanus & Strom, 1991; Saken, Fesen & Shull 1992). There are two reasons why our dust mass estimate is lower. First, the mass absorption coefficient for Mg protosilicate is about a factor of 2 larger than that applied in the other studies. Second and more importantly, the dust temperature we find is significantly higher than those estimated from the *IRAS* observations. Part of this difference is the high temperature implied when fitting the data with Mg protosilicate emissivity (cf. Figs. 3 and 4c), and part of the difference is that the SWS data do not include the 60 and $100 \mu\text{m}$ and are therefore insensitive to the presence of cooler dust grains in the FMKs or elsewhere in the SNR.

The apparent excess of 60 and $100 \mu\text{m}$ emission in Figure 3 suggests the presence of a second, cooler dust component in the Cas A SNR. A fit to the 60 and $100 \mu\text{m}$ flux densities only gives a dust temperature of 52 K (Arendt 1989), and a resulting cool dust mass of $\sim 3.8 \times 10^{-2} M_{\odot}$ for the entire SNR. (Note that masses quoted by Arendt 1989 are too large by a factor of π .) The $25 \mu\text{m}$ emission of this cooler dust would be ~ 18 Jy or $\sim 10\%$ of the total emission. This contribution would not greatly alter the spectral fitting discussed previously.

3.2.2. Dust Heating and Location

The collisional heating rate for a dust grain of radius a (in cm) is given by (Dwek 1987):

$$H_{\text{coll}}(a, T_e) = \pi a^2 \left(\frac{32}{\pi m_e} \right)^{1/2} n_e (kT_e)^{3/2} h(a, T_e) \quad (2)$$

where m_e , n_e , and T_e are the electron mass, number density, and temperature, and $h(a, T_e)$ is a grain heating efficiency, which approaches a value of ~ 1.0 for larger grains and lower temperatures. The radiative heating rate of the same dust grain can be expressed as:

$$H_{\text{rad}}(a) = \pi a^2 \langle Q_{\nu} \rangle cU \quad (3)$$

where U is the radiative energy density and $\langle Q_{\nu} \rangle$ denotes the spectrally averaged absorption coefficient. In the region immediately behind a shock passing through a FMK, we can approximate the energy density as $U = \frac{1}{c} \int I d\omega = \frac{1}{c} l n_e^2 \Lambda$ where l is a mean scale length of the emitting region (e.g. the cooling length of the shock), and Λ is the cooling function of the shocked gas in units of $\text{erg cm}^3 \text{ s}^{-1}$. The ratio of these heating rates is thus

$$\frac{H_{\text{coll}}}{H_{\text{rad}}} = \left(\frac{32kT_e}{m_e c^2} \right)^{1/2} \frac{n_e kT_e h(a, T_e)}{U \langle Q_{\nu} \rangle} \quad (4)$$

The sum of these heating rates will be equal to the grain cooling rate or luminosity:

$$L_{\text{gr}} = 4\pi a^2 \sigma T_d^4 \langle Q(a, T_d) \rangle \quad (5)$$

where T_d is the dust temperature, and $\langle Q(a, T_d) \rangle$ is the dust absorption coefficient averaged over a Planck spectrum of temperate T_d .

Equating the grain heating and cooling rates, we can solve for the grain temperature given estimates to the gas temperature, density, and cooling function. Sutherland & Dopita (1995) present models of the

structure and emission from shocked knots of O-rich ejecta. Hurford & Fesen (1996) suggest that these models with cloud shock velocities of $\sim 150 - 200 \text{ km s}^{-1}$ may be appropriate for the Cas A FMKs, if the extinction is ~ 1 mag greater than the commonly adopted $A_V = 4.3$ mag (Searle 1971). Thus, the 200 km s^{-1} shock model of Sutherland & Dopita (1995) estimates a postshock temperature of $T_e = 10^{6.64} \text{ K}$, $n_e = 400 \text{ cm}^{-3}$, and $\Lambda = 10^{-17.5} \text{ erg cm}^3 \text{ s}^{-1}$. For these conditions, collisional heating dominates radiative heating by factors of several hundred, and the dust temperature is given by

$$T_d = \left[\frac{\left(\frac{32}{\pi m_e}\right)^{1/2} n_e (kT_e)^{3/2} h(a, T_e)}{4\sigma \langle Q \rangle} \right]^{1/4}. \quad (6)$$

For silicate grains with $T_d > 150 \text{ K}$, $\langle Q \rangle = 0.25 (a/1 \mu\text{m})$ (Draine & Lee 1984). Approximating $h \approx 1.0$, the estimated temperature for $a = 0.01 \mu\text{m}$ grains will be $T_d \approx 180 \text{ K}$. Larger grains will be correspondingly cooler. This simple calculation shows that the high dust temperature indicated by the continuum spectrum of Cas A is consistent with emission from collisionally heated dust in the post shock region of FMKs, but not with radiatively heated dust in the FMKs. Note that the collisional heating mechanism is only tenable if the electron temperature equilibrates with the ion temperature as in the models presented by Sutherland & Dopita (1995), in contrast to some of the pure oxygen shock models calculated by Itoh (1988) where electron temperatures only reach $T_e \approx 10^5 \text{ K}$.

In Region N3, the integrated flux of thermal emission from the hot dust is ~ 3 times the total flux in IR, optical, and UV lines, assuming that Hurford & Fesen (1996) FMK5 corresponds to the observed knot, and that the spectrum of Sutherland & Dopita’s OSP200 is a reasonable estimate of the UV line intensities. This suggests that thermal radiation from collisionally heated dust is the most important cooling mechanism for the shocked FMKs, in agreement with the more general comparison of the relative importance of X-ray and IR cooling found by Dwek et al. (1987b) for various SNRs.

While the hot dust appears to be associated with the FMKs, the location of the cooler dust producing the 60 and 100 μm emission is not as clear. If the cooler dust component is also associated with the FMKs, it could be dust within the unshocked (or cooled post-shock) volume of the FMKs. In a cooler environment, collisional heating of the dust may no longer be significant, but the radiation of the shock passing through a typical FMK may be sufficient to heat nearby dust to the required temperature of $T_d \approx 50 \text{ K}$. In this case, the ratio of the mass of hot dust to the mass of cool dust ($\sim 1/500$) will be equal to the fraction of the FMK mass that is contained within the hot post-shock region. However, the global 60 and 100 μm emission depicted in Fig. 3 may not originate in the FMKs. It may be emitted by dust in the X-ray emitting gas between and around the FMKs. A dust temperature of $\sim 50 \text{ K}$ would then imply electron densities of $\sim 1 \text{ cm}^{-3}$ if the dust grains have radii of $a = 0.1 \mu\text{m}$ (Dwek 1987). Higher electron densities would be required if the grains are larger. This derived density is not atypical for SNRs, but is somewhat low compared to some recent estimates of the density, $n_{e,t} \sim 100 \times 10^{11} \text{ cm}^{-3}$, derived from the X-ray observations of Cas A (Holt et al. 1994; Vink, Kaastra, & Bleeker 1996; Favata et al. 1997).

3.2.3. A Stochastic Heating Alternative

In the previous sections, the correlation of the continuum emission with the line emission of the FMKs is taken as evidence for dust radiating at equilibrium temperatures of $\sim 170 \text{ K}$ and collisionally heated by the shocked FMK gas. The composition of the dust appears to reinforce this conclusion. However, an alternate model for the strength and morphology of the continuum emission can be constructed, assuming

that the bulk of the dust is embedded in within the X-ray emitting gas rather than the FMKs. In this case, as *IRAS* observations had indicated, most of the dust is collisionally heated to temperatures of ~ 100 K in the hot X-ray emitting portion of the SNR. Then in regions where the FMKs are plowing into the reverse shock, the bowshocks of the knots compress the gas which will increase the dust temperatures and the spatial density of dust grains (Sutherland & Dopita 1995). However, this environment is at a significantly lower density than the material of the FMKs. Therefore, if the dust grains are small enough they will be stochastically heated, i.e. the grain cooling time will be shorter than the collision time, and the grain temperatures will fluctuate instead of remaining at equilibrium temperatures. From the work of Dwek (1986), we see that silicate grains with radii of $a = 0.005 \mu\text{m}$ immersed in a gas with $n_e = 10 \text{ cm}^{-3}$ and $T_e = 10^7$ K will have dust temperatures $30 < T_{dust} < 200$ K. The presence of the colder grains leads to additional emission at longer wavelengths. For the example chosen here, this improves the fit between the model and the SWS and KAO data (dashed line in Fig. 3).

While dust heated in the bow shocks of the FMKs may be responsible for the correlation of the optical FMKs with the brightest emission in the $11.3 \mu\text{m}$ image (Lagage et al. 1996), the fainter diffuse emission that forms a nearly complete shell correlates fairly well with both X-ray and radio emission (e.g. Anderson & Rudnick 1995). This shell would be emission from stochastically heated dust grains in the lower density X-ray emitting gas. In addition, the shell could contain significant synchrotron emission, depending on the actual shape of the extension of the radio synchrotron spectrum into the IR regime (e.g. Mezger et al. 1986; Dwek et al. 1987a; Tuffs et al. 1998). The morphology of the X-ray and radio emission are similar after correction for extinction (Keohane, Rudnick & Anderson 1996; Keohane, Gotthelf, & Petre 1998), making it difficult to distinguish thermal from synchrotron emission by the apparent structure.

4. DISCUSSION

4.1. Mixing of the Ejecta

On a large scale, the Cas A SNR gives the impression of a star that has been dissected by layers. First, most of the H- and N-rich outer layers are lost in winds prior to the SN explosion, leading to the QSFs (van den Bergh 1971; Peimbert & van den Bergh 1971). Then, in the SN explosion, the outermost layer of the star is blasted away at the highest velocity, producing the N-rich FMFs (Fesen, Becker, & Blair 1987; Fesen, Becker, & Goodrich 1988). Inner layers of the star produce the FMKs, some of which are mainly oxygen, and others, from deeper layers of the star, contaminated with O-burning products (Si, Ar, Ca) (Chevalier & Kirshner 1979; Winkler, Roberts, & Kirshner 1991). All of these knots of ejecta are rendered visible when they are shocked in the expanding shell of the SNR blast wave. The QSFs are caught by the shell, at the forward shock; the fast-moving knots and flocculi catch the decelerating shell from the inside, at the reverse shock.

Within this framework, the lack of [Ar II] emission from the South regions (§3.1) suggests that the material in this region originated in layers of the star above the O-burning zone. The observed ejecta is presumably trailed by ejecta enriched with O-burning products which has yet to catch up with the reverse shock because either the knots have lower velocities or the reverse shock is located at a larger radius than in the northern portion of the SNR. Additional suggestions of a lack of mixing in the SN ejecta are provided by the composition of the dust, discussed below.

Despite the large scale differentiation of the ejecta, evidence for partial mixing of the ejecta is provided by the observation of [Fe II] and [Ni II] in optical spectra of FMKs (e.g. Winkler, Roberts, & Kirshner

1991), and now by the detection of IR lines of both Ne and Ar in the FMK spectra in the North regions of the SNR (Lagage et al. 1996; Tuffs et al. 1998). The argon, iron, and nickel originate in layers of the progenitor that lie below the oxygen-burning shell, whereas the neon is found in layers above the oxygen-burning shell (Weaver, Zimmerman & Woosley 1978; Woosley, Axelrod, & Weaver 1984; Johnston & Yahil 1984).

4.2. Dust Formation in the Ejecta

Since the Cas A SNR is still sweeping up the circumstellar material shed by its progenitor, the dust in the SNR must be relatively recently formed either in the pre-SN stellar wind, or from the ejecta of the SN itself. The correlation of the continuum intensity with the O and Ar line strengths of the FMKs suggest that the observed dust has formed from the ejecta. In §3.2, we found that the continuum spectrum is well represented by dust with optical properties similar to those the Mg protosilicates measured in the lab by Dorschner et al. (1980). We favor the Mg over the Ca and Fe protosilicates because of the good match to the position and width of the 22 μm emission feature, and because the Mg abundance should exceed the Ca and Fe abundances in the O-rich layers of evolved massive stars (Weaver et al. 1978; Woosley et al. 1984), with no mixing of the ejecta required. Similar mixing considerations have led Clayton et al. (1997) to propose that type X SiC grains found in meteorites must originate in type Ia SNe, rather than type Ib or II SNe as Cas A is generally believed to be. We also favor the Mg protosilicate identification of the dust over the possibility of FeO dust, because while FeO dust could create the 22 μm feature, its spectrum drops quickly at $\lambda > 25 \mu\text{m}$ and would still require another dust component to provide the longer wavelength emission seen in the SWS spectra and in the *IRAS* data. Finally, the 400 K dust temperatures required for the FeO grains is higher than we expect to find in the SNR at this time.

The apparent presence of Mg protosilicates does not preclude the presence of carbonaceous dust which may have formed in the ejecta. The fate of C in the Cas A ejecta is difficult to determine. Normally strong C lines are obscured by high extinction at UV wavelengths, optical lines are weak (Hurford & Fesen 1996), and no C lines are present in the spectral range of the SWS. If the carbon is locked up in graphitic dust, its IR spectrum will lack any distinctive features in contrast to the strong spectral features of silicate grains. The composition of the dust required to explain the 60 and 100 μm emission seen by the *IRAS* is unconstrained by the broadband observations. This dust component could be either additional silicate dust or carbonaceous dust since only a fraction of the carbon in the ejecta is expected to be locked up in CO molecules (Clayton, Liu, & Dalgarno 1998).

5. Conclusion

The *ISO* SWS data have allowed a detailed look at the line and continuum emission from the Cas A SNR. The data provide new information on the composition of both the gas and dust in the supernova ejecta. The line emission is dominated by [O IV] 25.89 μm , which is not surprising for this prototype of oxygen-rich SNRs. Emission from oxygen-burning products, particularly [Ar II] 7.99 μm , is also strong in some regions of the SNR. The dust composition revealed by these data clearly show that the dust formed in the ejecta differs from typical interstellar silicates. A Mg protosilicate composition is suggested for the recently formed dust. The mass of the hot dust observed appears to be a small fraction of the condensible silicon. However, a cooler dust component is also present in the SNR, though not necessarily associated

with the FMKs.

Somewhat unexpectedly, the SWS data do not provide evidence for emission from iron in the SN ejecta, in either the gas phase or the dust. Another unresolved question concerns the apparent morphological differences that are implied between the 20 – 25 μm emission observed with the SWS and previous *IRAS* and ground-based studies (Dwek et al. 1987a; Greidanus & Strom 1991).

We wish to thank A. Noriega-Crespo, S. Unger, and the IPAC staff for help with data reduction. R. Smith, W. Glaccum, and K.-W. Chan provided useful assistance with the KAO data and its interpretation. We thank H. Mutschke and the group at Friedrich-Schiller-Universität Jena for making their optical data available on the internet. This analysis was funded through NASA’s ISO Guest Observer program.

REFERENCES

- Anderson, M. C., & Rudnick, L. 1995, *ApJ*, 441, 307
- Arendt, R. G. 1989, *ApJS*, 70, 181
- Baade, W., & Minkowski, R. 1954, *ApJ*, 119, 206
- Bohren, C. F., & Huffman, D. R. 1983, *Absorption and Scattering of Light by Small Particles*, (New York: Wiley)
- Braun, R. 1987, *A&A*, 171, 233
- Butler, K., & Mendoza, C. 1984, *MNRAS*, 208, 17P
- Chevalier, R. A., & Kirshner, R. P. 1979, *ApJ*, 233, 154
- Clayton, D. D., Arnett, D., Kane, J., & Meyer, B. S. 1997, *ApJ*, 486, 824
- Clayton, D. D., Liu, W., & Dalgarno, A. 1998, *Science*, in press
- de Graauw, T., et al. 1996, *A&A*, 315, L49
- Dinerstein, H. L., Capps, R. W., Dwek, E., & Werner, M. W. 1982, *ApJ*, 255, 552
- Dinerstein, H. L., Lester, D. F., Rank, D. M., Werner, M. W., & Wooden, D., H. 1987, *ApJ*, 312, 314
- Dorschner, J., Friedmann, C., Guertler, J., & Duley, W. W. 1980, *Ap&SS*, 68 159
- Draine, B. T., & Lee, H. M. 1984, *ApJ*, 285, 89
- Dwek, E. 1986, *ApJ*, 302, 363
- Dwek, E. 1987, *ApJ*, 322, 812
- Dwek, E., & Arendt, R. G. 1992, *ARA&A*, 30, 11
- Dwek, E., Dinerstein, H. L., Gillett, F. C., Hauser, M. G., & Rice, W. L. 1987a, *ApJ*, 315, 571
- Dwek, E., Petre, R., Szymkowiak, A., & Rice, W. L. 1987b, *ApJ*, 320, L27
- Dwek, E., & Werner, M. W. 1981, *ApJ*, 248, 138
- Favata, F., Vink, J., Dal Fiume, D., Parmar, A. N., Santangelo, A., Mineo, T., Preite-Martinez, A., Kaastra, J. S., & Bleeker, J. A. M. 1997, *A&A*, 324, L49
- Fesen, R. A., Becker, R. H., & Blair, W. P. 1987, *ApJ*, 313, 378
- Fesen, R. A., Becker, R. H., & Goodrich, R. W. 1988, *ApJ*, 329, L89

- Fesen, R. A. 1990, *AJ*, 99, 1904
- Greidanus, H., & Strom, R. G. 1991, *A&A*, 249, 521
- Henning, Th., Begemann, B., Mutschke, H., & Dorschner, J. 1995, *A&AS*, 112, 143
- Holt, S. S., Gotthelf, E. V., Tsunemi, H., & Negoro, H. 1994, *PASP*, 46, L151
- Houck, J., R., Shure, M. A., Gull, G. E., & Herter, T. 1984, *ApJ*, 287, L11
- Hurford, A. P., & Fesen, R. A. 1996, *ApJ*, 469, 246
- Itoh, H. 1988, *PASJ*, 33, 1
- Johnston, M. D., & Yahil, A. 1984, *ApJ*, 285, 587
- Keenan, F. P., & Conlon, E. S. 1993, *ApJ*, 410, 426
- Kelsall, T., et al. 1998, *ApJ*, 508, 44
- Keohane, J. W., Gotthelf, E. V., & Petre, R. 1998, *ApJ*, 503, L175
- Keohane, J. W., Rudnick, L., & Anderson, M. C. 1996, *ApJ*, 466, 309
- Lagage, P. O., Claret, A., Ballet, J., Boulanger, F., Césarsky, C. J., Césarsky, D., Fransson, C., & Pollock, A. 1996, *A&A*, 315, L273
- Mathis, J. S. 1990, *ARA&A*, 28, 37
- Mezger, P. G., Tuffs, R. J., Chini, R., Kreysa, E., & Gemünd, H.-P. 1986, *A&A*, 167, 145
- Moseley, H., Arendt, R., Dwek, E., Casey, S. C., Chan, K. W., Glaccum, W. J., Graham, J., Loewenstein, R. F., & Smith, R. 1993, *BAAS*, 25, 851
- Peimbert, M., & van den Bergh, S. 1971, *ApJ*, 167, 223
- Reed, J. E., Hester, J. J., Fabian, A. C., & Winkler, P. F. 1995, *ApJ*, 440, 706
- Saken, J. M., Fesen, R. A., & Shull, J. M. 1992, *ApJS*, 81, 715
- Searle, L. 1971, *ApJ*, 168, 41
- Sutherland, R. S., & Dopita, M. A. 1995, *ApJ*, 439, 381
- Tuffs, R. J., Drury, L. O’C., Rasmussen, I., Heinrichsen, I., Innes, D. E., Russell, S., Schnopper, H., & Völk, H. J. 1998, in preparation
- van den Bergh, S. 1971, *ApJ*, 165, 457
- Vink, J., Kaastra, J. S., & Bleeker, J. A. M. 1996, *A&A*, 307, L41
- Weaver, T. A., Zimmerman, G. B., & Woosley, S. E. 1978, *ApJ*, 225, 1021
- Winkler, P. F., Roberts, P. F., & Kirshner, R. P. 1991, in *Supernovae. The 10th Santa Cruz Workshop in Astronomy and Astrophysics*, ed. S. E. Woosley, (New York: Springer-Verlag), 652
- Woosley, S. E., Axelrod, T. S., & Weaver, T. A. 1984, in *Stellar Nucleosynthesis*, ed. C. Chiosi & A. Renzini, (Dordrecht: D. Reidel), 263
- Wright, E. L., Harper, D. A., Loewenstein, R. F., Keene, J., & Whitcomb, S. E. 1980, *ApJ*, 240, L157